

AIAA 81-0565R

Nonlinear Dynamic Phenomena in the Space Shuttle Thermal Protection System

J. M. Housner*

NASA Langley Research Center, Hampton, Va.

H. H. Edighoffer†

General Electric Corporation, Philadelphia, Pa.

and

K.C. Park‡

Lockheed Palo Alto Research Laboratory, Palo Alto, Calif.

The development of an analysis for examining the nonlinear dynamic phenomena arising in the Space Shuttle orbiter tile/pad thermal protection system is presented. The tile/pad system consists of ceramic tiles bonded to the aluminum skin of the orbiter through a thin nylon felt pad. The pads are a soft nonlinear material which permits large strains and displays both hysteretic and nonlinear viscous damping. Application of the analysis to a square tile subjected to sinusoidal motion of the orbiter skin is presented and the following nonlinear dynamic phenomena are considered: highly distorted waveforms; amplitude-dependent resonant frequencies which initially decrease and then increase with increasing amplitude of motion; magnification of substrate motion, which is higher than would be expected in a similarly highly damped linear system; and classical parametric resonance instability.

Nomenclature

A	= amplitude of vertical sinusoidal substrate acceleration	T	= period of steady-state motion
A_p	= tile/pad contact area	T_0	= applied tile torque about z axis
C_x, C_y, C_z	= damping coefficients, see Eqs. (14)	u, v, w	= displacement components in x, y, and z directions, respectively
E_{xx}, E_{yy}, E_{zz}	= components of the Green strain tensor	u_0, v_0, w_0	= values of u, v, and w at tile centroid, respectively
f, f_e	= magnification factors defined in Eqs. (33) and (36)	u_s, v_s, w_s	= components of substrate displacements in x, y, and z directions, respectively
$\{F\}$	= applied tile force vector, see Eq. (24)	V_p	= undeformed pad volume
F_u, F_v	= applied tile centroidal forces in x and y directions, respectively	x, y	= lateral axes, see Fig. 1
G	= acceleration due to gravity	z	= vertical axis (normal to orbiter skin), see Fig. 1
h_p, h_t	= pad and tile thicknesses, respectively	α_x, α_y	= rotation of tile about x and y axes, respectively
K_x, K_y, K_z	= effective stiffness coefficients in nonlinear viscous damping law, see Eq. (15)	β_x, β_y	= average linear pad rotations as defined in Eq. (21)
m	= tile mass	ϵ	= linear vertical strain component as defined in Eq. (20)
$[M]$	= system mass matrix, see Eq. (22)	γ_x, γ_y	= linear shear strain components as defined in Eq. (20)
M_x, M_y	= applied moments about x and y axes, respectively	η	= loss factor defined in Eq. (29)
P	= applied tile centroidal normal force in z direction	θ	= rotation about z axis
$\{q\}$	= vector of tile displacement components defined in Eq. (23)	σ_a	= uniform applied normal stress
q_n, q_s	= damping law exponents, see Eq. (13)	$\sigma_{xx}, \tau_{xx}, \tau_{zy}$	= Euler stress components
$\{Q\}$	= vector of internal pad stress resultants defined in Eq. (19)	τ_a	= applied uniform shear stress
r_x, r_y, r_z	= tile radii of gyration about x, y, and z axes, respectively	ω_n, ω_s	= low-amplitude, steady-state vertical and lateral resonant frequencies about fixed normal and shear prestress states, respectively
S_{xx}, S_{xy}, S_{yy}	= Kirchhoff stress components	Ω	= frequency of sinusoidal substrate motion
S_{zx}, S_{zy}, S_{zz}	= Kirchhoff stress components	$\Omega_r, \bar{\Omega}$	= reference and resonant frequencies
$\bar{S}_{xx}, \bar{S}_{xy}, \bar{S}_{yy}$	= steady-state, time-averaged Kirchhoff stress components	ζ	= coefficient of nonlinear viscous damper, see Eq. (14)
t	= time	ζ_e	= equivalent quasilinear percent of critical damping ratio as given by Eq. (35)

Presented as Paper 81-0565 at the AIAA/ASME/ASCE/AHS 22nd Structures, Structural Dynamics & Materials Conference, Atlanta, Ga., April 9-10, 1981; submitted April 8, 1981; revision received Oct. 27, 1981. This paper is declared a work of the U.S. Government and therefore is in the public domain.

*Aerospace Engineer, Structures and Dynamics Division.

†Senior Engineer, Re-entry Systems Division.

‡Staff Scientist, Applied Mechanics Laboratory.

Subscripts and Superscripts

D	= strain-rate-dependent stresses
I	= strain-rate-independent stresses
o	= tile centroid
p	= pad
s	= substrate
(\cdot)	= $\partial(\cdot)/\partial t$

Introduction

THE Space Shuttle orbiter thermal protection system consists of ceramic tiles bonded to thin nylon felt pads, known as strain isolator pads, which are composed of thousands of intertwined nylon filaments. The pads, in turn, are bonded to the aluminum skin of the Shuttle orbiter. During a mission, tile/pad combinations experience dynamic loads arising from acoustics, structural vibration, and transonic shock. As a consequence, the pad experiences motion of varying magnitudes and frequencies. Experiments¹ have shown that as the pad is cyclically loaded and unloaded, hysteresis loops occur in the stress-strain behavior of the material. Furthermore, these loops creep as a function of stress level and number of cycles. The creep of the loops eventually becomes very small with each additional cycle, but its effect is to produce a highly nonlinear hardening pad material which is quite soft at low stress levels and considerably stiffer at higher stress levels. In addition, the hardened material exhibits both coulomb- and viscous-type damping. For tiles under static load² and for the unidirectional response of tiles under dynamic load,³ it was found that the nonlinear pad material properties after cycling significantly affected tile/pad behavior. This produced, in many cases, considerably higher normal stresses in the pad than before cycling. The nonlinear pad properties also give rise to certain physical phenomena of both practical and academic interest.

The purpose of this paper is to present a synopsis of the different analytically predicted nonlinear dynamic phenomena which arise in the Space Shuttle tile/pad thermal protection system and the development of the analytical model used in their prediction. The following phenomena will be considered:

- 1) highly distorted waveforms having sharp high stress peaks;
- 2) amplitude-dependent resonant frequencies which initially decrease and then increase with increasing amplitude of motion;
- 3) higher amplification of imposed substrate motion than would be expected in a similarly highly damped linear system; and
- 4) classical parametric resonance due to large tile motion.

All of these phenomena have been observed in laboratory tests of sinusoidally driven tile/pad combinations and where available are compared with predicted responses. Although flight dynamic loads are expected to be random, the system nonlinearities should be understood and characterized under sinusoidal loading before examination of more complex loading.

Tile, Substrate, and Pad Motions

As shown in Fig. 1, the tile/pad Space Shuttle thermal protection system consists of ceramic tiles bonded to the Space Shuttle aluminum skin (substrate) through a felt pad. In deriving a mathematical model for the system, a series of assumptions are made for the tile, substrate, and pad motions.

Assumption 1

For the tile, it is assumed, as in Refs. 2 and 3, that each tile behaves as a rigid body and undergoes small rotations. Consequently, the tile displacements u_t , v_t , and w_t parallel to the x , y , and z axes, respectively, as shown in Fig. 1, may be expressed as

$$\begin{aligned} u_t(y, z, t) &= u_0(t) + z\alpha_y(t) - y\theta(t) \\ v_t(x, z, t) &= v_0(t) - z\alpha_x(t) + x\theta(t) \\ w_t(x, y, t) &= w_0(t) + y\alpha_x(t) - x\alpha_y(t) \end{aligned} \quad (1)$$

Assumption 2

The substrate is assumed to have lateral rigid body motions $u_s(t)$ and $v_s(t)$ and vertical motion $w_s(x, y, t)$ due to substrate flexibility.

Assumption 3

For the pad, the following linear through-the-thickness displacements are assumed:

$$\begin{aligned} u_p(y, z, t) &= \frac{[u_t(y - h_t/2, t) - u_s(t)]z'}{h_p} + u_s(t) \\ v_p(x, z, t) &= \frac{[v_t(x - h_t/2, t) - v_s(t)]z'}{h_p} + v_s(t) \\ w_p(x, y, z, t) &= \frac{[w_t(x, y, t) - w_s(x, y, t)]z'}{h_p} + w_s(x, y, t) \end{aligned} \quad (2)$$

where

$$z' = h_p + h_t/2 + z$$

Substituting Eq. (1) into Eq. (2) gives

$$\begin{aligned} u_p &= \frac{(u_0 - h_t\alpha_y/2 - y\theta - u_s)z'}{h_p} + u_s \\ v_p &= \frac{(v_0 + h_t\alpha_x/2 + x\theta - v_s)z'}{h_p} + v_s \\ w_p &= \frac{(w_0 + y\alpha_x - x\alpha_y - w_s)z'}{h_p} + w_s \end{aligned} \quad (3)$$

Constitutive Law for the Pad

General Discussion of Pad Stress-Strain Behavior

Assumption 4

Because the pad is known to be a very soft material, it is anticipated that pad deformations and strains will be large. Consequently, it is elected to establish the pad constitutive law in terms of Kirchhoff stresses and Green strains.⁵ Inasmuch as the pad experiences only tensile, compressive, and shear load applied to its surface normal to the z axis, it is reasonable to assume that the following Kirchhoff stress components vanish:

$$S_{xx} = S_{yy} = S_{xy} = 0 \quad (4)$$

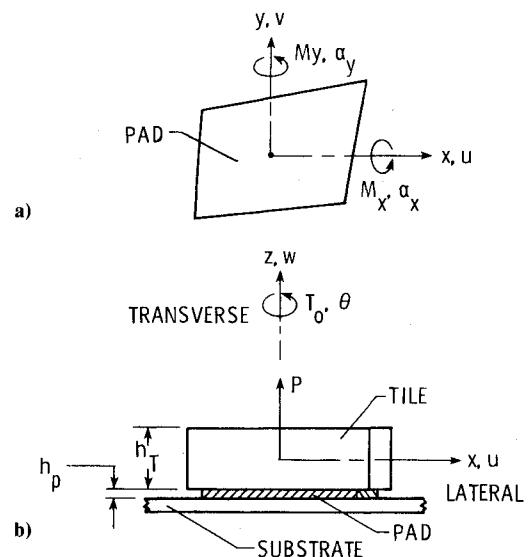


Fig. 1 Tile/pad geometry. a) Tile/pad contact area; b) Tile/pad/substrate profile.

Assumption 5

For the nonvanishing stresses, material property tests¹ were conducted in which the pad was slowly loaded in tension, compression, or shear on its surface normal to the z axis. These tests revealed, as displayed in Figs. 2a and 2b, that under cyclic loading of a prescribed amplitude the pad exhibits hysteretic behavior. The hysteresis loops thus formed involve energy dissipation and may be due to static coulomb frictional damping which is strain-rate independent. This is physically reasonable since pad filaments are sliding over one another during loading or unloading. However, it is known⁴ that for a driven linear spring/mass/damper system, the energy dissipation due to coulomb damping is not sufficient to produce bounded oscillations at resonant frequencies. Inasmuch as physical oscillations are always bounded, it would appear reasonable to postulate an additional energy dissipation mechanism which is strain-rate dependent. Thus it is assumed that the total pad Kirchhoff stress components are the algebraic sum of strain-rate-independent and strain-rate-dependent components denoted by superscripts (I) and (D) , respectively. Thus

$$\begin{aligned} S_{zz} &= S_{zz}^{(I)} + S_{zz}^{(D)} \\ S_{zx} &= S_{zx}^{(I)} + S_{zx}^{(D)} \\ S_{zy} &= S_{zy}^{(I)} + S_{zy}^{(D)} \end{aligned} \quad (5)$$

When the strain rate goes to zero, the superscript (D) terms vanish and the slow load-rate hysteresis becomes the sole damping mechanism. From the formulas of Ref. 5 and

elsewhere, the Euler (or actual) stresses in the deformed pad may be calculated from the Kirchhoff stresses of the deformed pad using Eqs. (2).

Assumption 6

It is further assumed for the pad constitutive law that the strain-rate-independent Kirchhoff stress components depend upon the history of the Green strain components E_{zz} , E_{zx} , and E_{zy} , while the strain-rate-dependent Kirchhoff stress components depend upon the strain-rate temporal derivatives \dot{E}_{zz} , \dot{E}_{zx} , and \dot{E}_{zy} . Substituting Eq. (3) into the definition of the Green strain tensor,⁵ the strain components may be expressed as

$$\begin{aligned} E_{zz} &= \frac{(w_0 + y\alpha_x - x\alpha_y - w_s)}{h_p} + \frac{1/2 (u_0 - h_t\alpha_y/2 - y\theta - u_s)^2}{h_p^2} \\ &\quad + \frac{1/2 (v_0 + h_t\alpha_x/2 + x\theta - v_s)^2}{h_p^2} + \frac{1/2 (w_0 + y\alpha_x - x\alpha_y - w_s)^2}{h_p^2} \\ 2E_{zx} &= \frac{(u_0 - h_t\alpha_y/2 - y\theta - u_s)}{h_p} + \frac{1/2\theta (v_0 + h_t\alpha_x/2 + x\theta - v_s)}{h_p} \\ &\quad + 1/2 (\partial w_s / \partial x - \alpha_y) \left[1 + \frac{(w_0 + y\alpha_x - x\alpha_y - w_s)}{h_p} \right] \\ 2E_{zy} &= \frac{(v_0 + h_t\alpha_x/2 + x\theta - v_s)}{h_p} - \frac{1/2\theta (u_0 - h_t\alpha_y/2 - y\theta - u_s)}{h_p} \\ &\quad + 1/2 (\partial w_s / \partial y + \alpha_x) \left[1 + \frac{(w_0 + y\alpha_x - x\alpha_y - w_s)}{h_p} \right] \end{aligned} \quad (6)$$

where E_{zx} and E_{zy} have been approximated by using average values over the pad thickness.

Strain-Rate-Independent Stresses**Assumption 7: Conditioning of the Pad**

As shown in Figs. 2a and 2b, the hysteresis loops under slow cyclic loading creep as a function of load amplitude and number of cycles. As is the case with many materials, the primary creep range in which the creep is rapid is followed by a secondary range in which the creep is much slower. Hence the creep of the loop eventually becomes very small with additional load cycles of the same or lower amplitude. This process, which produces a quasistabilized material will be referred to as "conditioning." The hysteresis loop formed by the conditioning load cycles will be referred to as the loop "envelope." Provided the pad has not experienced a load amplitude higher than the one conditioned at, it would appear that the creep of the hysteresis loops can be safely neglected during a short time analysis. Hence it is assumed that the pad material has been conditioned at a load amplitude which is not exceeded during the period of time to be analyzed. Analytical responses of the system have indicated that the system is not very sensitive to small additional creeping. As a consequence of this assumption, the analysis may be carried out over a small period of time (e.g., a few hundred cycles) and then restarted using material property data corresponding to additional cycles at the calculated stress amplitudes which meet or exceed the conditioning amplitude. Consider then the conditioned envelopes arising under uniaxial tension/compression and shear cyclic tests.

Uniaxial Tests and Assumption 8

The uniaxial tension/compression tests measure the relationship between an applied uniform normal stress, σ_a , and displacement, w_0/h_p , as shown in Fig. 2a. In these tests, the Euler stresses are

$$\sigma_{zz} = \sigma_a \quad \tau_{zx} = \tau_{zy} = 0 \quad (7)$$

while u_s , v_s , and w_s are zero.

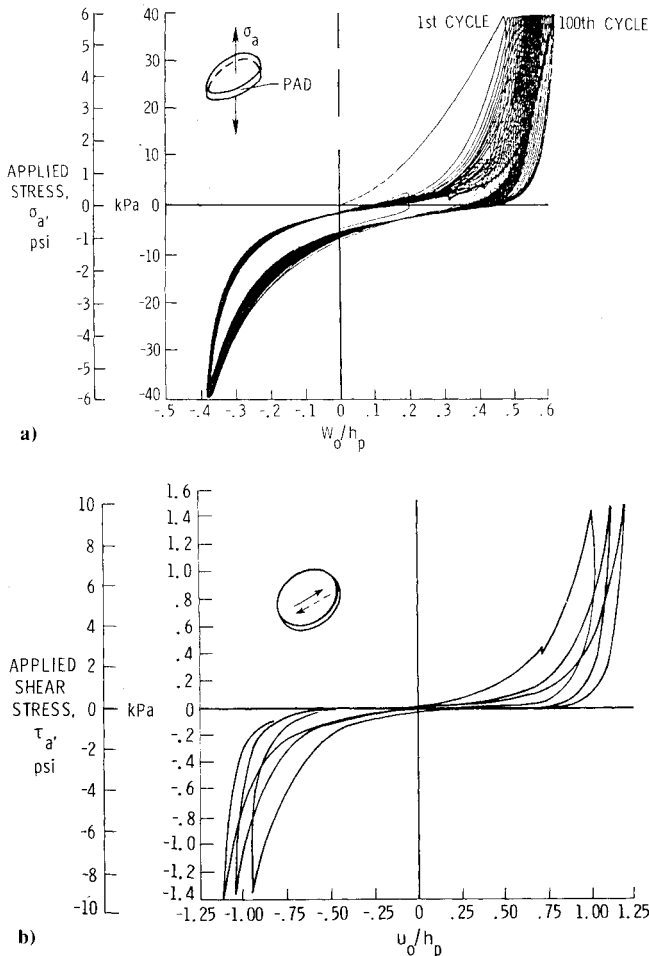


Fig. 2a) Effect of uniaxial cyclic loading on through-the-thickness pad material properties; b) effect of cyclic shear loading on pad material shearing properties.

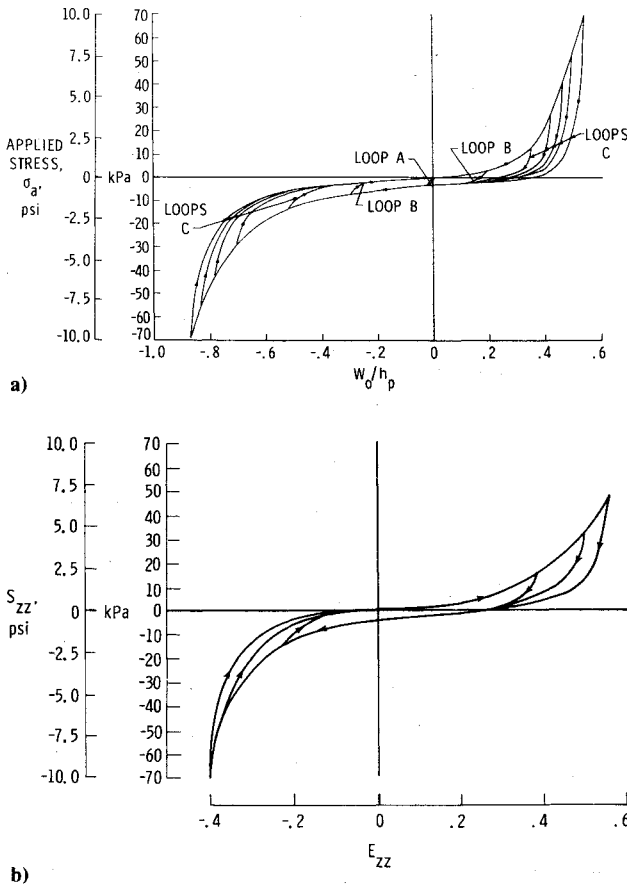


Fig. 3a) Loading/unloading paths within a conditioned hysteresis envelope during uniaxial test; b) loading/unloading paths within a conditioned hysteresis envelope for coupled vertical-lateral motions.

A typical envelope resulting from the uniaxial cyclic loading is shown in Fig. 3a. Also shown are typical loading and unloading paths from different strain-rate-independent states within and on the envelope. Based on the observations of pad behavior and on assumption 7, it is further assumed that, irrespective of loading or unloading path, the pad strain-rate-independent state cannot lie outside of the envelope and that within the envelope loading/unloading paths may be curve fitted by appropriate scaling and translation of portions of the envelope. However, as discussed later, the presence of strain-rate-dependent stresses allows the total stress-strain state to lie outside the envelope. Details on the curve fitting are given in Ref. 3.

In the uniaxial tests the strain-rate-independent Kirchhoff stress components are

$$S_{zz}^{(I)} = \sigma_a / (1 + w_0/h_p) \quad S_{zx}^{(I)} = S_{zy}^{(I)} = 0 \quad (8)$$

Also, by symmetry, u_0 , v_0 , α_x , α_y , and θ are zero, so that from Eq. (6)

$$E_{zx} = E_{zy} = 0 \quad E_{zz} = w_0 [1 + (1/2) w_0/h_p] / h_p \quad (9)$$

Hence, for uniaxial loading, an empirical relationship between S_{zz} and E_{zz} as presented in Fig. 3b may be established from the uniaxial test curves of Fig. 3a and Eqs. (8) and (9).

Shear Tests and Assumption 9

The cyclic shear tests measure the relationship between an applied uniform shear stress, τ_a , parallel to the x (or y axis), and the displacement u_0/h_p (or v_0/h_p). Assuming that the material is isotropic in the x - y plane, there is no loss in

generality to consider the Euler (or actual) stress state as

$$\tau_{zx} = \tau_a \quad \tau_{zy} = \sigma_{zz} = 0 \quad (10)$$

while u_s , v_s , and w_s are also zero. From cyclic shear tests a typical envelope and loading/unloading paths from different strain-rate-independent states may be established similar to what is done for the uniaxial tests. Assumption 8 is also taken to apply to the shear tests.

In the shear tests the Kirchhoff stresses are

$$S_{zz}^{(I)} = S_{zy}^{(I)} = 0 \quad S_{zx}^{(I)} = \tau_{zx}^{(I)} = \sigma_a \quad (11)$$

and by symmetry, v_0 , w_0 , α_x , α_y , and θ are zero, so that from Eq. (3),

$$2E_{zx} = u_0/h_p \quad E_{zz} = w_0/h_p + 1/2 u_0^2/h_p^2 + 1/2 w_0^2/h_p^2 \quad (12)$$

Hence the relationship between S_{zx} and $2E_{zx}$ (or similarly S_{zy} and $2E_{zy}$) is the same as that shown in Fig. 2b for τ_a vs u_0/h_p .

Assumption 10: Coupling of Normal and Lateral Motions

Tests have shown that an applied stress, σ_a , affects the relationship between τ_a and u_0/h_p , and likewise τ_a affects the relationship between σ_a and w_0/h_p . For example, when the pad is sheared in the absence of σ_a , Figs. 4a and 4b show that a coupling exists between w_0/h_p and τ_a . This coupling may be adequately analyzed by modeling the pad behavior to account for large displacements rather than resorting to a coupled constitutive law which would be difficult to experimentally quantify. Hence it is assumed that there is no coupling in the pad constitutive law; that is, $S_{zz}^{(I)}$ depends solely upon the strain history of E_{zz} ; $S_{zx}^{(I)}$ depends solely upon the strain history of E_{zx} ; and $S_{zy}^{(I)}$ depends solely upon the strain history of E_{zy} . This assumption allows the constitutive law governing the strain-rate-independent stress components $S_{zz}^{(I)}$, $S_{zx}^{(I)}$, and $S_{zy}^{(I)}$ to be determined solely from uniaxial compression/tension and shear test data since all the coupling is provided by the geometric large displacement terms in the strain components.

Since $S_{zz}^{(I)}$ is zero during the shear test, the use of this assumption implies that E_{zz} must also be zero during the shear test. However, the test data imply that E_{zz} actually has a small value during the shear tests as shown in Fig. 4b. This figure displays the actual test value of E_{zz} , which is calculated at different values of the applied shear stress τ_a using the second of Eqs. (12), the shear test envelope, and the measured normal motions of the pad during the shear test as shown in Fig. 4a. From Fig. 4b it is seen that a relatively small vertical normal strain exists compared to the lateral shear strain during the shear test. As shown in Fig. 3a, S_{zz} is quite small at small values of E_{zz} . Thus assumption 10 appears to be quite reasonable.

Assumption 11: Strain-Rate-Dependent Stresses

It is assumed that the strain-rate-dependent stress components are given by a power law in which each dissipative stress component is in the direction of the corresponding strain-rate component as³

$$\begin{aligned} S_{zx}^{(D)} &= C_x h_p \dot{E}_{zx} |2\pi \dot{E}_{zx} / \Omega_r|^{q_s-1} / A_p \\ S_{zy}^{(D)} &= C_y h_p \dot{E}_{zy} |2\pi \dot{E}_{zy} / \Omega_r|^{q_s-1} / A_p \\ S_{zz}^{(D)} &= C_z h_p \dot{E}_{zz} |2\pi \dot{E}_{zz} / \Omega_r|^{q_n-1} / A_p \end{aligned} \quad (13)$$

where Ω_r is a fixed reference frequency; q_n and q_s are damping parameter exponents to be determined from test; and C_x , C_y , and C_z are assumed to be proportional to an effective dynamic stiffness, such that

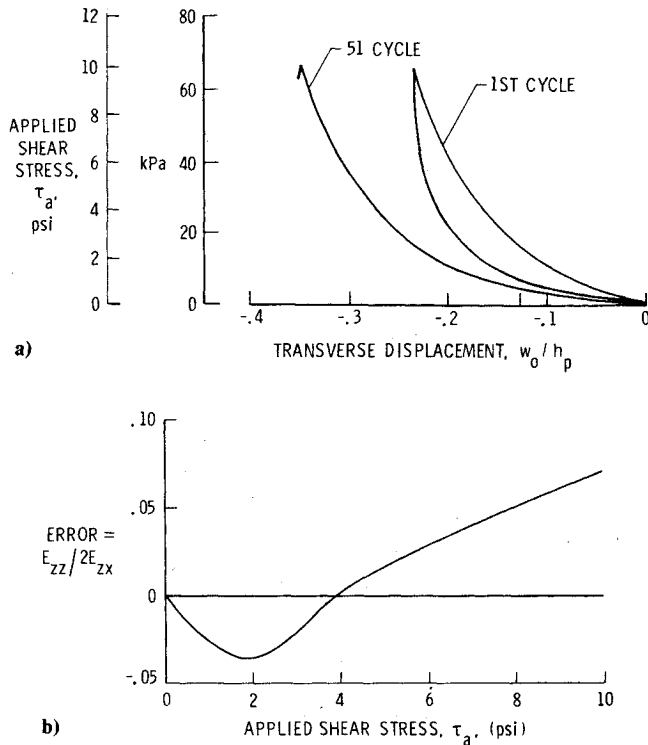


Fig. 4a) Vertical motion of pad due to applied cyclic shear stress; b) error generated in approximating vertical-lateral coupling.

dynamic stiffness, such that

$$C_x = 2K_x \zeta_s / \Omega_r \quad C_y = 2K_y \zeta_s / \Omega_r \quad C_z = 2K_z \zeta_n / \Omega_r \quad (14)$$

in which ζ_n and ζ_s are dimensionless damping parameters to be determined from tests. Owing to the coulomb frictional forces present in the pad, the pad stiffness properties are discontinuous at the strain-rate reversals that occur during cyclic motion. Hence it is reasonable to define K_x , K_y , and K_z as effective dynamic stiffnesses which are stress dependent; that is,

$$K_x = m\omega_s^2 [\bar{S}_{zx}^{(I)}] \quad K_y = m\omega_s^2 [\bar{S}_{zy}^{(I)}] \quad K_z = m\omega_n^2 [\bar{S}_{zz}^{(I)}] \quad (15)$$

where ω_n and ω_s are low amplitude resonant frequencies about mean stress levels, \bar{S}_{zz} , \bar{S}_{zx} , \bar{S}_{zy} , of the fluctuating components of pad stress. The frequencies ω_n and ω_s may be determined on the basis of low amplitude sinusoidal uniaxial and shear tests, respectively, about prestress conditions in the pad. Furthermore, it is convenient to select the reference frequency, Ω_r , equal to the vertical low amplitude resonant frequency about a zero mean stress level in an actual tile/pad system[§]

$$\Omega_r = \omega_n [0] \quad (16)$$

In Eq. (13) a single term representation of the strain-rate-dependent stress components is used rather than a sum of such terms since it is highly desirable to keep the number of parameters to be evaluated from tests to a minimum. The existence of the strain-rate-dependent stress components allows the total state of stress-strain to lie outside of the conditioned envelope.

[§]The tile/pad system considered herein consists of a 15.24 × 15.24 × 9.525-cm LI900 tile on a 12.7 × 12.7 × 0.406-cm pad (6 × 6 × 3.75-in. tile on a 5 × 5 × 0.160-in. pad). An LI900 tile has a mass density of 0.288 g/cm³ (9 lb/ft³).

Equations of Motion

The equations of motion may be derived from the principle of virtual work, which, in the undeformed geometry of the pad, may be expressed as

$$\int_{V_p} (S_{zz} \delta E_{zz} + 2S_{zx} \delta E_{zx} + 2S_{zy} \delta E_{zy}) dV_p + m(\ddot{u}_0 \delta u_0 + \ddot{v}_0 \delta v_0 + \ddot{w}_0 \delta w_0 + r_x^2 \ddot{\alpha}_x \delta \alpha_x + r_y^2 \ddot{\alpha}_y \delta \alpha_y + r_z^2 \ddot{\theta} \delta \theta) - [F_x \delta u_0 + F_y \delta v_0 + P \delta w_0 + M_x \delta \alpha_x + M_y \delta \alpha_y + T_0 \delta \theta] = 0 \quad (17)$$

where δ is the variational operator.

Substituting Eqs. (6) into Eq. (17) and recognizing that the resulting equations must be true for all variations of w_0 , u_0 , v_0 , α_x , α_y , and θ gives the following equations of motion:

$$\{Q\} + [M]\{\ddot{q}\} = \{F\} \quad (18)$$

where $\{Q\}$ is the internal resultant force vector whose components are

$$Q_1 = \int_{A_p} [S_{zz}(1 + \epsilon) + S_{zx}\beta_y + S_{zy}\beta_x] dA_p$$

$$Q_2 = \int_{A_p} [S_{zx} + \gamma_x S_{zz} - 1/2 \theta S_{zy}] dA_p$$

$$Q_3 = \int_{A_p} [S_{zy} + \gamma_y S_{zz} + 1/2 \theta S_{zx}] dA_p$$

$$Q_4 = \int_{A_p} \{y/h_p [(1 + \epsilon) S_{zz} + \beta_y S_{zx} + \beta_x S_{zy}] + 1/2 S_{zy}(1 + \epsilon)\} dA_p + 1/2 (h_T/h_p) Q_3$$

$$Q_5 = \int_{A_p} \{-x/h_p [(1 + \epsilon) S_{zz} + \beta_x S_{zy} + \beta_y S_{zx}] - 1/2 S_{zx}(1 + \epsilon)\} dA_p - 1/2 (h_T/h_p) Q_2$$

$$Q_6 = \int_{A_p} [S_{zz}(x\gamma_y - y\gamma_x)/h_p + 1/2 S_{zx}(\gamma_y + x\theta/h_p - 2y/h_p) + 1/2 S_{zy}(2x/h_p + \theta y/h_p - \gamma_x)] dA_p \quad (19)$$

where ϵ , γ_x , and γ_y are linear strain components

$$\epsilon = \frac{(w_0 + y\alpha_x - x\alpha_y - w_s)}{h_p}$$

$$\gamma_x = \frac{(u_0 - \alpha_y h_T/2 - y\theta - u_s)}{h_p} \quad (20)$$

$$\gamma_y = \frac{(v_0 + \alpha_x h_T/2 + x\theta - v_s)}{h_p}$$

and β_x and β_y are average rotational components,

$$\beta_x = 1/2 (\partial w_s / \partial y + \alpha_x) \quad \beta_y = 1/2 (\partial w_s / \partial x - \alpha_y) \quad (21)$$

$[M]$ is the diagonal mass matrix,

$$[M] = m \begin{bmatrix} 1 & & & & & \\ & 1 & & & & 0 \\ & & 1 & & & \\ & & & r_x^2/h_p^2 & & \\ & & & & r_y^2/h_p^2 & \\ 0 & & & & & r_z^2/h_p^2 \end{bmatrix} \quad (22)$$

$\{q\}$ is the vector of displacement components,

$$\{q\} = \begin{bmatrix} w_0 \\ u_0 \\ v_0 \\ \alpha_x h_p \\ \alpha_y h_p \\ \theta h_p \end{bmatrix} \quad (23)$$

and $\{F\}$ is the applied tile force vector,

$$\{F\} = \begin{bmatrix} P \\ F_x \\ F_y \\ M_x/h_p \\ M_y/h_p \\ T_0/h_p \end{bmatrix} \quad (24)$$

Equations (18) are integrated explicitly using the following recursive relations

$$\{\dot{q}\}_{i+1} = \{\dot{q}\}_i + \Delta t [M]^{-1} \{ \{F\}_i - \{Q\}_i \} \quad (25)$$

$$\{q\}_{i+1} = \{q\}_i + \Delta t \{\dot{q}\}_{i+1} \quad (26)$$

where Δt is an appropriate time step. The initial conditions for Eqs. (19) may be specified on the strain-rate-independent Kirchhoff stress components, on $\{q\}$, and on $\{\dot{q}\}$. The initial strains and strain rates may then be calculated from Eqs. (6) and the strain-rate-dependent stresses from Eq. (13). If the initial state of stress strain lies outside of the normal or shear envelope, then the strain rate must initially be nonzero.

At the i th time step, the known displacement vector $\{q\}_i$ and $\{\dot{q}\}_i$ are used to compute the Green strains and strain rates from Eq. (6). In turn, these strains and strain rates, in conjunction with Eqs. (5), (13), and the tracing of the stress-strain curves (see Ref. 3 for details on how the tracing of the stress-strain curves is accomplished on the computer), provide the Kirchhoff stresses. Integration of these stresses in Eq. (19) yields the resultant pad force vector at the i th time step $\{Q\}_i$. The velocity and displacement vectors are updated for the $i+1$ time step using Eqs. (25) and (26).

Vertical Sinusoidal Substrate Motion

General Discussion

In this paper application of the analysis presented herein is limited to a typical LI900 thick tile on the Space Shuttle.¶ Experimental results are from Refs. 3, 6, and 7.

It is believed that the primary source of dynamic excitation to the tile/pad system on the Space Shuttle orbiter is from vertical substrate motion. Hence, consider the case where $\{Q\}$ is zero and

$$w_s = (AG/\Omega^2) \sin \Omega t \quad (27)$$

while u_s and v_s are zero and A is the number of G 's of acceleration. For $S_{zz}^{(D)}$, the damping parameters were determined in Ref. 3 based on available test data to be

$$\zeta_n = 0.15 \quad q_n = 2 \quad (28)$$

$S_{zz}^{(D)}$ may then be found by substituting Eqs. (28) and (14) through (16) into the last of Eqs. (13).

Wave Shape

Figure 5 shows the analytically predicted and experimentally observed steady-state tile/pad interface stress, σ_{zz} , as a function of time due to the substrate motion described by Eq. (27), when A is 30 and Ω is 80 Hz. The Euler stress σ_{zz} may be calculated from the solution of Eqs. (25) and (26) as

$$\sigma_{zz} = (1 + w_0/h_p) S_{zz}$$

Both the analytical and experimental wave shapes are highly nonlinear with high stress peaks. (A linear system would give a purely sinusoidal response.) These peaks seem to be due to the tile acquiring a high velocity over the soft material range which causes it to overshoot into the stiff material range thus producing high stress peaks on each cycle of motion.

Resonant Frequency

Figure 6 displays the variation of resonant frequency $\bar{\Omega}$ with substrate acceleration amplitude A . $\bar{\Omega}$ is taken as that value of Ω which yields the peak amplitude steady-state pad stress. The experimental data were derived from tests on two tile/pad combinations. Variation in pad properties between the two specimens probably accounts for much of the data scatter. The analysis uses average pad data and thus lies within the data scatter. With increasing A , analysis and experiment both show a rapid decrease in resonant frequency (effective dynamic softening) followed by a slow increase in resonant frequency (effective dynamic hardening).

The trend can be understood by considering the material behavior of Fig. 3a. At small values of A the material follows a stiff loading/unloading loop (loop A), with little or no portion of the cycle on the lower modulus envelope. This indicates that for small A the friction forces between pad filaments account for the entire load carrying mechanism of the pad. As A is increased, a large portion of the cycle lies on the soft portion of the envelope (loop B), and so the resonant frequency decreases. With further increase in A , the resonant frequency starts increasing as more and more of the cycle begins to include the higher modulus region of the envelope at raised stress levels (loop C).

Pad Damping

Damping mechanisms in the pad may be examined by using the analysis to evaluate the loss factor η at the resonant steady-state frequency. The loss factor is defined herein as

$$\eta = (1/2\pi) (E_d/E_k) \quad (29)$$

where E_k is the peak kinetic energy attained by the tile during a steady-state cycle of motion, namely,

$$E_k = (1/2) m |\dot{w}_{\text{peak}}|^2 \quad (30)$$

and E_d is the energy dissipated by the pad per cycle of steady-state motion, which may be calculated by evaluating the integral

$$E_d = \int_{t_0}^{t_0+T} A_p \sigma_{zz} (\dot{w} - \dot{w}_s) dt \quad (31)$$

in which t_0 is any time large enough so that the system is in steady-state motion and T is the period of motion,

$$T = 2\pi/\bar{\Omega} \quad (32)$$

In Fig. 7 the variation of η with A is shown with and without nonlinear viscous damping present; that is, with both strain-rate-independent and -dependent stresses present, and

¶See footnote §.

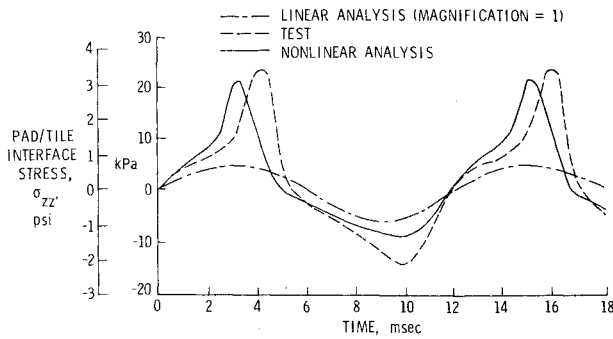


Fig. 5 Nonlinear wave shape due to sinusoidal substrate acceleration, $A=30$.

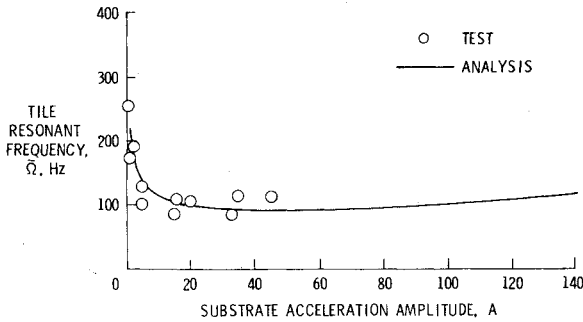


Fig. 6 Variation of tile resonant frequency with imposed vertical sinusoidal substrate acceleration amplitude.

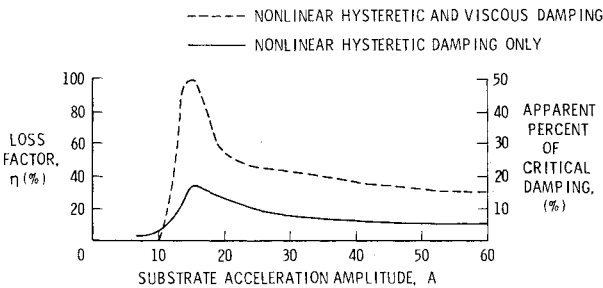


Fig. 7 Variation of loss factor with amplitude of vertical sinusoidal substrate acceleration.

with only strain-rate-independent stresses present. In the latter case, the energy dissipation is due only to hysteretic losses attributable to pad friction. Both curves exhibit similar trends and show η approaching a constant value at large values of A . For high values of A , it appears that the energy loss due to strain-rate-independent stresses alone accounts for about 30% of the total energy loss. Figure 7 also indicates that maximum energy dissipation efficiency occurs near a value of A equal to 15 (i.e., a substrate acceleration of about 15 G 's). This is reflected in the system magnification factor f , defined as,

$$f = |w| / |w_s| \quad (33)$$

which after substituting Eq. (27) into Eq. (33) yields

$$f = \ddot{w} / AG \quad (34)$$

Figure 8 illustrates the analytical and experimental variation of f with A and, as would be expected from Fig. 7, the analytical curve has a minimum when A is between 10 and 15, but, unfortunately, the scatter in the experimental data makes confirmation of this difficult.

Development of Equivalent Linear Viscous Damper

It has been shown that the tile/pad system is highly nonlinear. Nevertheless, it may be desirable to establish linear

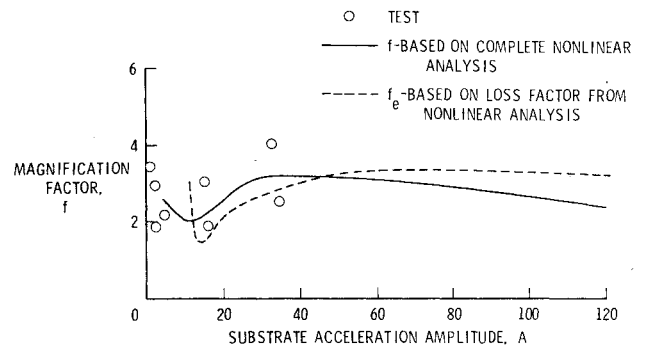


Fig. 8 Variation of magnification factor with amplitude of vertical sinusoidal substrate acceleration.

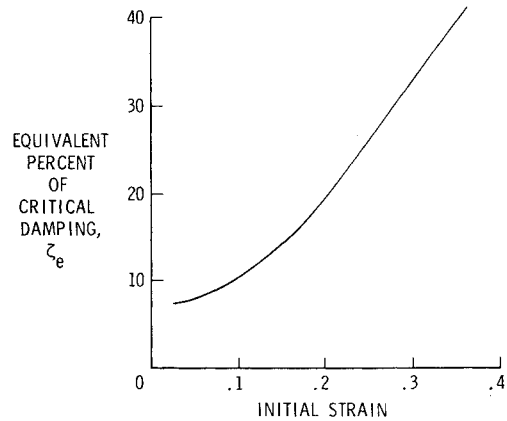


Fig. 9 Variation with initial strain of equivalent percent of critical damping ratio on the basis of logarithmic decrement.

models which can provide reasonable results for certain dynamic characteristics of the system. To this end an equivalent linear viscous damper is sought by using the nonlinear analysis to evaluate an equivalent percent of critical pad damping ratio denoted as ζ_e .

A typical procedure for determining ζ_e is based upon logarithmic decrement in which the pad is given an initial strain and then allowed to come to rest. This procedure provides an indication of the decay rate of tile response and is therefore significant in transient analysis. The logarithmic procedure gives⁸

$$\zeta_e = \Delta [(2\pi)^2 + \Delta^2]^{-1/2} \quad (35)$$

where

$$\Delta = \ln (w_{t=0} / w_{t=T})$$

Figure 9 provides the variation of ζ_e for different initial strains and shows that ζ_e increases monotonically with initial strain; going from 8% at small initial strain to over 40% at a relatively high initial strain. Since ζ_e varies significantly with initial strain, the log decrement procedure yields at best a quasilinear model in which the damping ratio would be provided as a prescribed strain-dependent variable.

Using ζ_e , an equivalent magnification factor, f_e , can be established at the resonant frequency using the linear result³

$$f_e = 1/2 (1/\zeta_e) [1 + 4\zeta_e^2]^{-1/2} \quad (36)$$

Thus, from Fig. 9 and Eq. (36), it is seen that f_e , when based on log decrement, decreases from 6.17 at small initial strain to about 1 at a relatively high initial strain. This observation does not correlate well with the nonlinearly predicted results of Fig. 8. For example, it is reasonable to believe that the value of f_e at high strain should correlate with the value at high substrate motion, but it does not. Thus, while the log

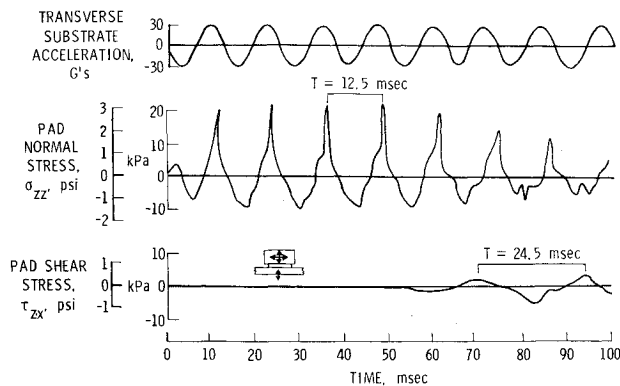


Fig. 10 Development of parametric resonance during vertical sinusoidal substrate motion.

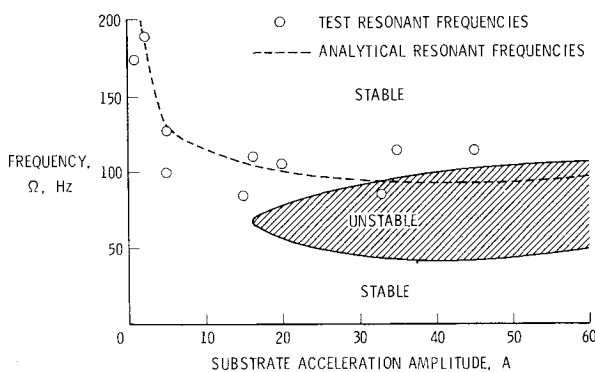


Fig. 11 Parametric resonance stability boundary.

decrement procedure indicates that large amplitude motion is highly damped and will decay rapidly, it leads to an underestimation of the magnification of substrate motion.

An alternate procedure for establishing ζ_e is based upon the loss factor η . An equivalent quasilinear viscous damper dissipates the same energy per cycle as the nonlinear system at the resonant frequency when ζ_e is one-half of the loss factor η .⁹ Since ζ_e varies with A in a manner similar to the variation of η with A (see Fig. 7), again a strictly linear equivalent viscous damper cannot be determined. However, ζ_e based on loss factor yields reasonable correlation with the nonlinearly predicted magnification factor as shown in Fig. 8, where Eq. (35) has been used to evaluate f_e based on loss factor.

In summary then, ζ_e based on logarithmic decrement is generally higher than that based on loss factor especially at high amplitude motions. Consequently, high response peaks decay rapidly with time, but energy dissipation in the pad is not consistently as high owing to the nonlinear character of the pad which allows the tile to accelerate rapidly through the soft modulus region of the pad and thus attain a high pad stress peak of short time duration in the stiff modulus region of the pad.

Parametric Resonance

At certain combinations of the vertical substrate acceleration amplitude A and the frequency Ω , the system becomes unstable laterally. This is demonstrated analytically in Fig. 10, where the substrate is oscillating vertically in steady-state motion at 80 Hz with an acceleration amplitude of A equal to 30 (i.e., 30 G's). If the system is perfectly symmetric, as is assumed here, no lateral motion occurs and the normal stress, σ_{zz} , exhibits the typical nonlinear high-peaked response history seen in Fig. 5, while the shear stress is zero. However, in reality there always exists some perturbing disturbance to excite an instability if it exists. Hence, to excite the lateral motion, a small oscillatory disturbing shear stress is

externally applied to the tile with a magnitude of 0.001 psi and oscillating at 80 Hz; the same frequency as the vertical motion. (This is equivalent to 0.03 G's of lateral acceleration on the tile.) After a few cycles the lateral stress grows from 0.001 psi to about 0.5 psi and takes on a frequency about half that of the vertical substrate and tile frequency. Such behavior is classically referred to as parametric resonance.¹⁰ Figure 10 also shows that as the shear stress and hence lateral motion grows, the normal stress decreases as energy leaves the vertical motion and goes into lateral motion.

Using the analysis herein, similar results can be generated for other combinations of A and Ω to produce the stability boundary shown in Fig. 11. The stability boundary is derived using average pad properties and thus tile/pad specimens may have somewhat different boundaries from what is shown here. However, general statements about its character can be safely made.

The figure illustrates that for low amplitude motion the system is always stable, but becomes unstable above a critical value of A which for the pad properties used herein is 16. The instability occurs over a specific frequency band; the width of the band growing slowly with increasing A . Further, for the tile/pad combination under examination here, there does not appear to be any instability possible at frequencies below 40 Hz independent of A .

Also shown in Fig. 11 is a duplicate of the experimental and analytical resonant frequency variation with A as provided in Fig. 6. As is seen, the analytically predicted resonant frequencies, for the pad properties used herein, lie outside of the unstable region for values of A less than 32. Above this value the resonant frequency will have little significance unless the tile is restrained from lateral motion. Most of the experimental resonant frequencies lie in the predicted stable region and, for A greater than 16, all but one test data point lie above the unstable region. Thus, in performing sine sweep tests to locate resonant frequencies, the unstable region may well be entered temporarily. Indeed this has been the experience in experimental investigations, where the parametric resonance of the system was first observed. In fact, parametric resonances were observed in torsional as well as lateral instabilities.

Concluding Remarks

An analysis has been presented for examining the nonlinear dynamic behavior of the tile/pad thermal protection system of the Space Shuttle orbiter. The analysis takes into account the nonlinear behavior of the pad including both hysteretic and nonlinear viscous damping as well as large strains and coupled vertical-lateral motions. It was shown that the steady-state motion of the system due to sinusoidal substrate motion results in high pad stresses due to the tile acquiring a high velocity in the soft region of the pad material which causes it to overshoot into the stiff region of the material. It was also shown that the resonant frequencies of the system initially decrease and then increase with increasing amplitude of motion and that magnification of the imposed substrate motion is higher than would be expected in a similarly highly damped linear system. Furthermore, the soft nature of the pad leads to large strains which may produce a parametric resonance instability in the system.

References

- ¹Sawyer, J.W. and Rummler, D.R., "Room Temperature Properties of Shuttle Thermal Protection System Materials," NASA TM-81786, April 1980.
- ²Housner, J.M. and Garcia, R., "Nonlinear Static TPS Analysis," NASA TM-81785, March 1980.
- ³Housner, J.M., Edighoffer, H.H., and Park, K.C., "Nonlinear Dynamic Response of a Uni-Directional Model for the Tile/Pad Space Shuttle Thermal Protection System," NASA TM-81901, Nov. 1980.
- ⁴Timoshenko, S., *Vibration Problems in Engineering*, 2nd ed., D. Van Nostrand Co., Inc., New York, 1937, pp. 57-61.

⁵Fung, Y.C., *Foundations of Solid Mechanics*, Prentice Hall, Inc., Englewood Cliffs, New Jersey, 1965, pp. 436-439.

⁶Miserentino, R., Pinson, L.D., and Leadbetter, S.A., "Some Space Shuttle Tile/Strain-Isolator-Pad Sinusoidal Vibration Tests," NASA TM-81853, July 1980.

⁷Miserentino, R., Pinson, L.D., and Leadbetter, S.A., "Some Vibration Characteristics of a Space Shuttle Tile/Strain-Isolator Pad System," SAE Paper 801129, Oct. 1980.

⁸Meirovitch, L., *Elements of Vibration Analysis*, McGraw Hill Book Co., New York, 1975, pp. 19-21.

⁹Ottens, H.H., "Mathematical Formulation of Damping for Structural Response Analysis," AGARD Conference Proceedings 277, *Damping Effects in Aerospace Structures*, April 1979.

¹⁰Bolotin, V.V., *The Dynamic Stability of Elastic Systems*, Holden Day, Inc., San Francisco, 1964, Chaps. 1 and 2.

From the AIAA Progress in Astronautics and Aeronautics Series...

ENTRY HEATING AND THERMAL PROTECTION—v. 69

HEAT TRANSFER, THERMAL CONTROL, AND HEAT PIPES—v. 70

Edited by Walter B. Olstad, NASA Headquarters

The era of space exploration and utilization that we are witnessing today could not have become reality without a host of evolutionary and even revolutionary advances in many technical areas. Thermophysics is certainly no exception. In fact, the interdisciplinary field of thermophysics plays a significant role in the life cycle of all space missions from launch, through operation in the space environment, to entry into the atmosphere of Earth or one of Earth's planetary neighbors. Thermal control has been and remains a prime design concern for all spacecraft. Although many noteworthy advances in thermal control technology can be cited, such as advanced thermal coatings, louvered space radiators, low-temperature phase-change material packages, heat pipes and thermal diodes, and computational thermal analysis techniques, new and more challenging problems continue to arise. The prospects are for increased, not diminished, demands on the skill and ingenuity of the thermal control engineer and for continued advancement in those fundamental discipline areas upon which he relies. It is hoped that these volumes will be useful references for those working in these fields who may wish to bring themselves up-to-date in the applications to spacecraft and a guide and inspiration to those who, in the future, will be faced with new and, as yet, unknown design challenges.

Volume 69—361 pp., 6 × 9, illus., \$22.00 Mem., \$37.50 List

Volume 70—393 pp., 6 × 9, illus., \$22.00 Mem., \$37.50 List

TO ORDER WRITE: Publications Dept., AIAA, 1290 Avenue of the Americas, New York, N.Y. 10104